Nuclear Inst. and Methods in Physics Research, A 1014 (2021) 165731

Contents lists available at ScienceDirect

Nuclear Inst. and Methods in Physics Research, A

journal homepage: www.elsevier.com/locate/nima

"Spiral COSAMI" — A Multi-Undulator Compact Source for Actinic Mask Inspection in the extreme ultraviolet range

Albin F. Wrulich, Andreas Streun *, Leonid Rivkin

Paul Scherrer Institut, 5232 Villigen, Switzerland

ARTICLE INFO

Keywords:
Compact storage ring
Extreme ultraviolet
Synchrotron
Coupling

ABSTRACT

A compact electron storage ring provides a bright, stable and reliable source of extreme ultraviolet (EUV) radiation for metrology applications in semiconductor industry. The COSAMI concept (COmpact Synchrotron for Actinic Mass Inspection) applied design principles and technology of modern diffraction limited light source storage rings to an EUV facility operating at 13.5 nm wavelength. Since floor space is an important issue in an industrial environment, we propose a lattice configuration where three (or more) recirculation turns are stacked vertically. We present a facility, called Spiral-COSAMI, which simultaneously serves multiple (three or more) EUV beamlines within about the same floor space of the original COSAMI, and using the same type of injector and the same set of diagnostics, radio-frequency and pulsed magnet devices. The increased period of revolution of the multiple turns mitigates the problem of ion trapping and relaxes specifications of injection kickers.

1. Introduction

COSAMI, a compact light source for actinic mask inspection with ptychography in the extreme ultraviolet (EUV) wavelength range has been presented in [1–3]. EUV lithography is considered to be the most cost-effective next generation method for sub-22 nm high-volume manufacturing of semiconductor devices. It is based on reflective optical components for both the projection optics and the mask. Mask inspection is a crucial element for the implementation of this technology. Compact storage rings with radiation either from bending magnets or wigglers have been proposed earlier. However, bending magnets or wigglers emit light with relatively low brightness and with a broad spectrum from which the required wavelength has to be filtered out. Moreover, the intensity is not constant due to the long intervals between subsequent injections into the storage ring and the decay of electron beam intensity in this interval of time.

The COSAMI concept in [1] overcomes this problem by means of an undulator instead of a bending magnet or wiggler. The resulting difficulties, due to the lower vertical gap of an undulator and the corresponding reduction of the beam lifetime, is solved by implementing top-up injection from a full energy booster synchrotron. This in turn also provides the intensity stability of the electron beam which is required for actinic mask inspection with Ptychography.

COSAMI is a single source facility for high performance undulator radiation. It is built up in a racetrack shape, which allows the implementation of one undulator in one of the two straight sections. The second straight section is required to host the injection system and the accelerating RF-cavity. If several experimental stations should be supplied by this facility, the beam has to be split by mirrors, which causes a loss in intensity. Since there is an upper limit for the intensity of the storage ring beam, the supply of several stations by one facility is limited.

In this report a concept is presented, which allows the generation of three independent EUV beams with high beam power by maintaining on the other side the size of the required floor space [4]. All photon beams have the same characteristics, regarding flux, brilliance and coherence as the single source COSAMI facility.

Three undulators of same type as described in Ref. [2] would be used: it has 16 mm period and 0.4 T peak field to emit 13.5 nm radiation on the fundamental at the beam energy of 430 MeV. With 200 periods (length 3.2 m) and 150 mA beam current, it provides a flux of $1.35 \cdot 10^{15}$ photons/s/0.1%BW (corresponding to 20 mW power) and a brightness of about $2 \cdot 10^{18}$ photons/s/mm^2/mrad ^{2}/0.1%BW [1]. Built as fixed-gap devices the height requirement for the undulators can be reduced to about 60 cm to enable vertical stacking.

Compared to the plane version of COSAMI, the lattice has been extended by one half cell in each arc in order to create a symmetry point in the arc center which is required for the minimization of the coupling effect.

Normally, a storage ring with small circumference is strongly suffering from ion trapping effects, since only a gap with a modest length can be introduced if the average beam current should remain constant.

* Corresponding author.
E-mail address: andreas.streun@psi.ch (A. Streun).

https://doi.org/10.1016/j.nima.2021.165731
Received 24 June 2021; Received in revised form 2 August 2021; Accepted 8 August 2021
Available online 12 August 2021
0168-9002/

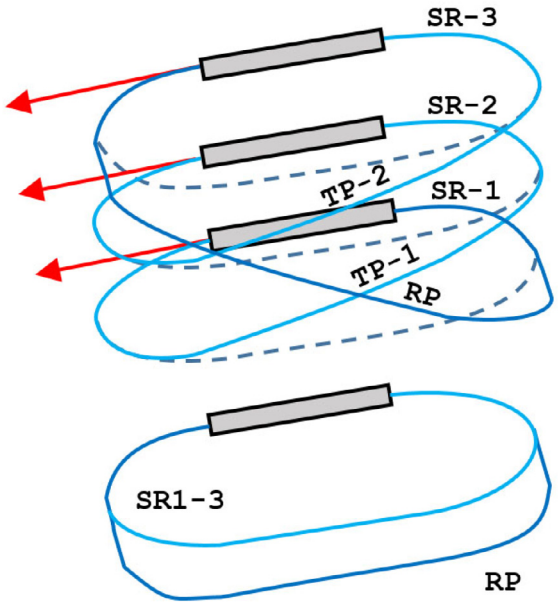

Fig. 1. Perspective view and top view of the spiral storage ring layout; SR: Storage Ring; TP: Transfer path; RP: Return path.

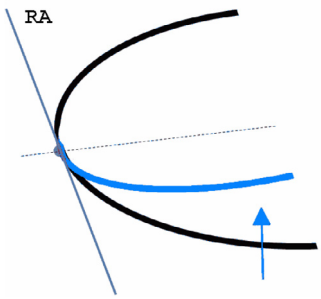

Fig. 2. Quarter arc rotation; RA: rotation axis for the quarter arc.

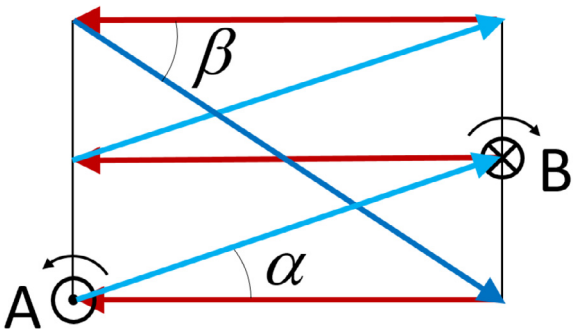

Fig. 3. Rotation angles of the half arcs; α: connection between 2 rings; β: return path from SR-3. The rotations by angle α at points A and B are in same direction (here: right hand screw).

For Spiral COSAMI on the other hand, for the same duty cycle a much longer gap is available which enhances the clearing efficiency.

Alternatively this concept could also be applied to any other compact source for which a small floor space is required and with different undulator types in the various loops. Obviously also the number of loops could be reduced or extended.

2. Basic layout for a spiral compact source with 3 undulators

The basic elements of the spiral source are three identical storage rings positioned on top of each other, which are interconnected in a spiral form. Each of the spiral loops is hosting an undulator which, if not used for actinic mask inspection, could be optimized for different wavelengths.

Fig. 1 shows the conceptual arrangement of such a facility. The three half rings in the back of the layout, positioned in the horizontal plane are hosting the 3 undulators. There is no special vertical deflection required to transport the beam from one level to the other. The quarter arcs in front are simply rotated in order to connect with the adjacent ring. For example, the left quarter arc in front of SR-1 is bent upwards, whereas the right quarter arc of SR-2 is bent downwards as shown in Fig. 2. The same configuration is implemented between SR-2 and SR-3.

For the return arc from SR-3 to SR-1 the half arc is laterally displaced in order to not interfere with the front structure of the rings. The conceptual front view of the 3-ring spiral with the return path is shown in Fig. 3. Assuming a separation between the rings of 0.75 m, the inclination angles of the transfer paths and the return path become roughly $\alpha = 3.8°$ and $\beta = 7.5°$.

3. Minimization of the transverse coupling

In a planar arrangement the horizontal and vertical betatron motions are uncoupled if no magnet errors are taken into consideration. This is not the case anymore for the baseline design of the spiral storage ring. In the following the requirements for a minimization of the coupling effects are derived.

The coupling is created in the inclined half rings of the transfer paths and the return path. In the transfer path the plane of motion is rotated by α at the beginning of the half ring (point A) and again by α at its end (point B).

The transformation matrix for the betatron oscillations from A → B is then given by:

$$\boldsymbol{M} = \boldsymbol{R}_\alpha \boldsymbol{M}_{xy} \boldsymbol{R}_\alpha = \begin{bmatrix} \cos\alpha & 0 & \sin\alpha & 0 \\ 0 & \cos\alpha & 0 & \sin\alpha \\ -\sin\alpha & 0 & \cos\alpha & 0 \\ 0 & -\sin\alpha & 0 & \cos\alpha \end{bmatrix} \begin{bmatrix} C_x & S_x & 0 & 0 \\ C'_x & S'_x & 0 & 0 \\ 0 & 0 & C_y & S_y \\ 0 & 0 & C'_y & S'_y \end{bmatrix} \times \begin{bmatrix} \cos\alpha & 0 & \sin\alpha & 0 \\ 0 & \cos\alpha & 0 & \sin\alpha \\ -\sin\alpha & 0 & \cos\alpha & 0 \\ 0 & -\sin\alpha & 0 & \cos\alpha \end{bmatrix} \quad (1)$$

Since A and B are optical symmetry points (with zero slopes) of a mirror symmetric arc, the betatron transformation matrices simplify to

$$\boldsymbol{M}_i = \begin{bmatrix} C_i & S_i \\ C'_i & S'_i \end{bmatrix} = \begin{bmatrix} \cos\mu_i & \beta_i \sin\mu_i \\ -\left(\frac{1}{\beta_i}\right)\sin\mu_i & \cos\mu_i \end{bmatrix} \quad (\mathrm{i} = \mathrm{x}, \mathrm{y}) \quad (2)$$

For small inclination angles, as it is the case here, we can neglect quadratic and higher order terms of α and we are left with the transformation matrix

$$\boldsymbol{M}_{xy} = \begin{bmatrix} \boldsymbol{M}_x & \boldsymbol{U}_\alpha \\ -\boldsymbol{U}_\alpha & \boldsymbol{M}_y \end{bmatrix},$$

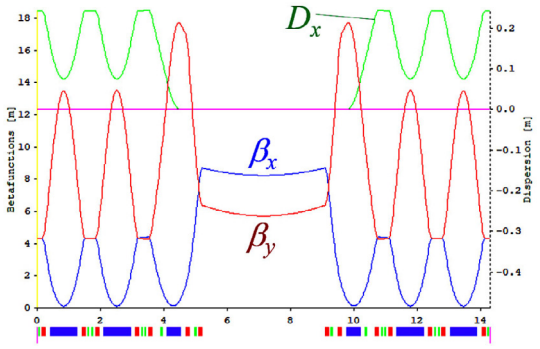

Fig. 4. Tilted half arc with dispersion and equal horizontal and vertical beta functions at the arc symmetry point for coupling compensation.

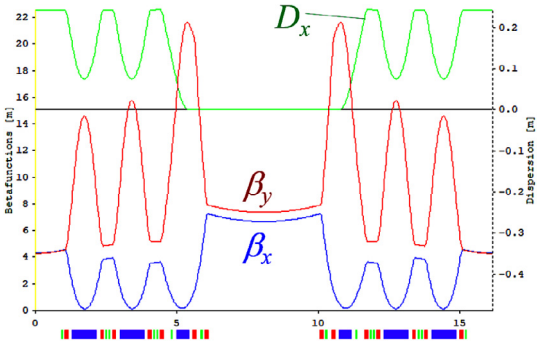

Fig. 5. Beta functions and dispersion of the return half loop.

$$U_\alpha = \begin{bmatrix} (\cos\mu_x + \cos\mu_y)\sin\alpha\cos\alpha & \left(\beta_x \sin\mu_x + \beta_y \sin\mu_y\right)\sin\alpha\cos\alpha \\ -\left(\frac{1}{\beta_x}\sin\mu_x + \frac{1}{\beta_y}\sin\mu_y\right)\sin\alpha\cos\alpha & (\cos\mu_x + \cos\mu_y)\sin\alpha\cos\alpha \end{bmatrix} \tag{3}$$

The elements in the skew diagonal vanish for an optics with $\beta_x = \beta_y$ at the rotation points A and B, and if in addition the horizontal phase advance between A and B is by an odd multiple of π larger than the vertical one, i.e. $\mu_x = \mu_y + k \times \pi$ (k = odd integer).

4. Storage ring lattice

4.1. Optics of half arcs for minimum coupling

Transfer half loop

The inclined half loop for the beam transfer to the next level (in the front of Fig. 1) will host the injection system whereas the planar back half loop (in the back of Fig. 1) will accommodate the undulators. For the plane of injection, a higher beta value is preferred.

Fig. 4 shows the optical functions and the lattice structure for the transfer half loop with an inclination angle of $\alpha = 3.86°$. A high degree of coupling compensation is reached for $\mu_x/2\pi = 2.731$ and $\mu_y/2\pi = 0.323$. Horizontal and vertical beta values are identical at the optical symmetry point, i.e. $\beta_x = \beta_y = 4.3$ m.

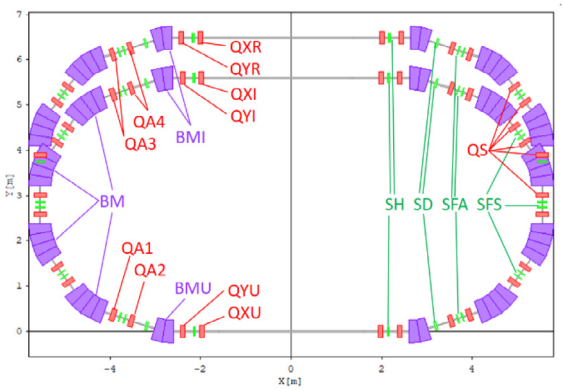

Fig. 7. Top view of the spiral storage ring with displaced return path.

The coupling matrix is given by $\mathbf{U}_\alpha = \begin{bmatrix} -0.0378 & -0.0279 \\ 0.0015 & -0.0378 \end{bmatrix}$.

The requirements for a strong horizontal focusing and equal beta functions at the symmetry points are in conflict with a perfect phase adjustment for a full linear coupling compensation. But as demonstrated by the skew matrix $\mathbf{U}_\alpha$, the results are quite satisfactory.

Return half loop

The half loop of the return path transfers the beam from the top loop to the bottom loop and needs to be transversely displaced in order not to interfere with the transfer paths. A displacement of 96 cm has been inserted at the symmetry point which leads to a harmonic number of $h = 146$ for a 500 MHz RF-system.

Fig. 5 shows the optics of the transfer half loop with additional 96 cm drift lengths on both sides.

The required return angle is $\beta = -7.69°$. Compensation is reached for $\mu_x/2\pi = 2.765$ and $\mu_y/2\pi = 0.339$. Horizontal and vertical beta values are identical at the optical symmetry point, i.e. $\beta_x = \beta_y = 4.3$ m.

The coupling matrix is given by $\mathbf{U}_\beta = \begin{bmatrix} -0.0578 & -0.0846 \\ 0.0046 & -0.0578 \end{bmatrix}$.

4.2. Spiral storage ring optics

The optics of one spiral loop with undulator is displayed in Fig. 6. There, the beta functions in the straight sections have been matched for maximum brilliance of the radiation.

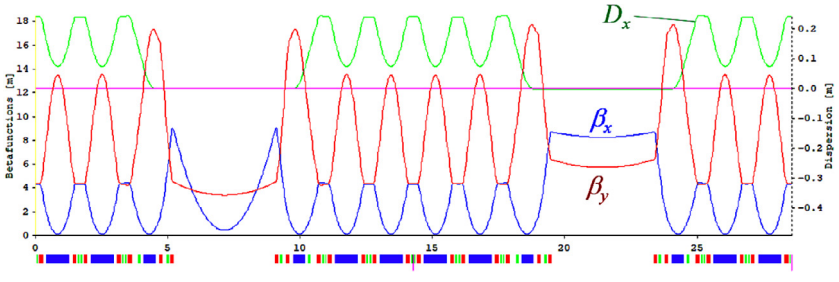

Fig. 6. One spiral loop with 2 straight sections. Left for the implementation of an undulator and right for the injection system.

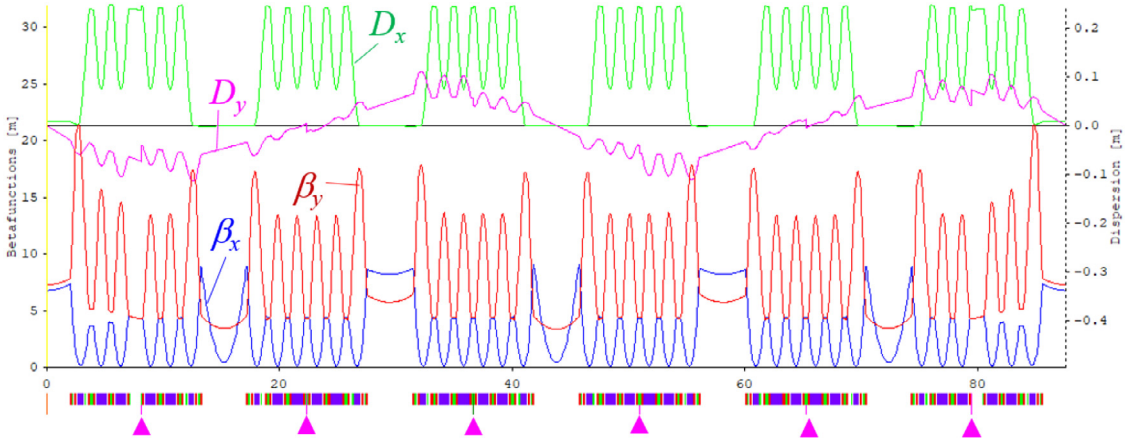

Fig. 8. Periodic optics of the complete spiral starting from the center of the return path. The six triangle markers at the bottom indicate the points of rotation by angles $-\beta$, α, α, α, α, $-\beta$ with $\alpha = 3.8635°$, $\beta = 7.6921°$.

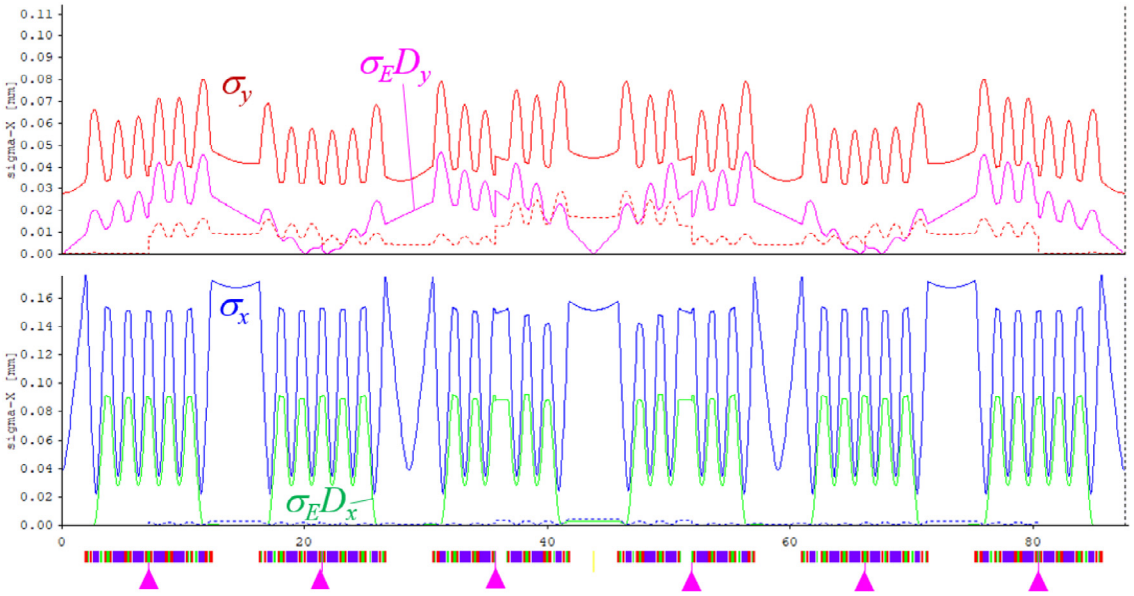

Fig. 9. Beam size (rms) around the ring, vertical (top) and horizontal (bottom), also showing the contributions from dispersion. Dotted lines indicate the contributions due to coupling from the other plane. The discontinuities (steps) in the curves are due to the rotation of the coordinate system of reference.

Table 1
Basic spiral storage ring parameters.

Parameter	Unit	Value
Footprint of the storage ring	m^2	12 × 7
Circumference	m	87.6
Beam energy	MeV	430
Injection		Full energy top-up
Intensity stability	%	0.1
Tunes Q_x/Q_y		17.48/2.15
Natural chromaticities ξ_x/ξ_y		−41.2/−32.3
Momentum compaction α_c	10^{-3}	18.6
Natural emittances ϵ_x/ϵ_y	nm rad	3.43/0.20
Energy loss per turn	keV	6.8
Energy spread	10^{-3}	0.372
Damping partition numbers $J_x/J_y/J_s$		1.531/1.002/1.476
Damping times $\tau_x/\tau_y/\tau_s$	ms	24.2/36.9/25.2

Finally all lattice sections are combined into a full ring. Rotation angles and distances are fine-adjusted to close the ring while maintaining exact values of circumference and vertical separation of undulators. A top view of the spiral storage ring is shown in Fig. 7. The required floor space is roughly 12 m × 7 m.

The arc of each loop is composed of 4 regular cells, a matching section with half bend and 4 quadrupoles, symmetrically arranged, for shaping the beta values in the straight sections. The quadrupoles and combined function magnets are different for the straight sections of the undulator and the transfer section. Among the inclined half loops, the return path has slightly modified quadrupole strengths as compared to the transfer path.

The coupled optics of the complete spiral storage ring is shown in Fig. 8, starting from the symmetry point of the straight section of the return path, and Fig. 9 shows the beam radii around the ring: Source size at the undulator centers is about 40 × 30 μm^2 rms.

The corresponding storage ring parameters are listed in Table 1.

5. Dynamic aperture

The main sextupoles for chromaticity correction are lumped elements (SFS) close to the horizontal focusing cell quadrupoles and integrated sextupoles in all cell bending magnets (BM), as shown in Fig. 10.

For driving term compensation sextupoles have also been placed in the straight section (SH) and close to the half bend where the

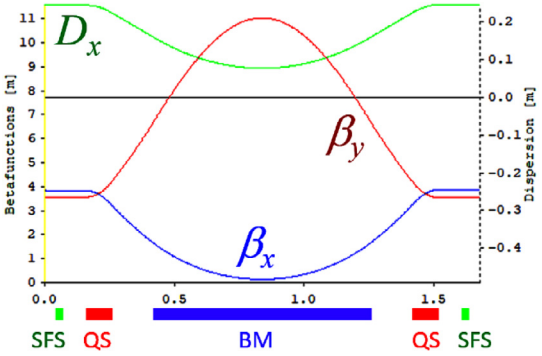

Fig. 10. Regular lattice cell. Sextupoles have been implemented as lumped elements (SFS) close to the horizontal focusing quadrupoles QS and integrated in the vertical focusing bending magnet BM.

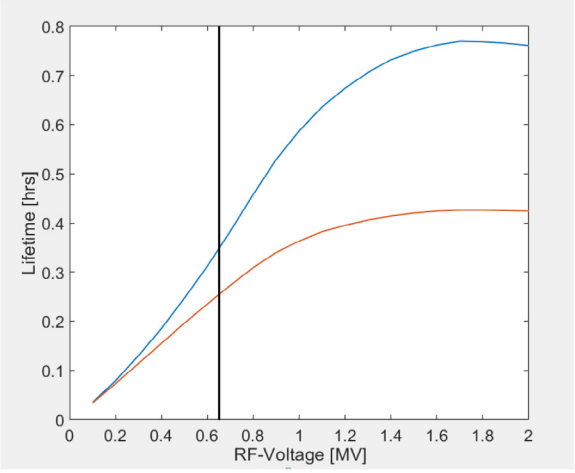

Fig. 12. Touschek lifetime (blue line, upper) and total lifetime (red line, lower) as a function of RF-voltage. With one cavity, the RF voltage is 650 kV as indicated by the vertical line. (For interpretation of the references to color in this figure legend, the reader is referred to the web version of this article.)

dispersion is matched to zero (SD). In addition, the sextupole strengths in the matching areas (SFA, BMI, BMU) have been used to optimize the dynamic aperture. Their strengths are collected in Table 4. The pattern of bending magnet and sextupole families is indicated in Fig. 7.

The resulting dynamic aperture for the symmetry point of the medium level undulator is displayed in Fig. 11 without and with undulator gaps.

6. Beam lifetime

The beam lifetime of Spiral COSAMI is mainly affected by elastic beam gas scattering and Touschek scattering. Inelastic beam gas scattering does not generate a relevant contribution.

The lifetime from elastic gas scattering is mainly defined by the small vertical gap of 6 mm in the undulator region. The loss rate due to Touschek scattering is proportional to the particle density in the bunch, and it is a steep inverse function of the momentum acceptance, which allows scattered particles to be captured. The momentum acceptance is defined by the RF voltage or the off-momentum lattice acceptance. Touschek lifetime as a function of RF voltage exhibits a maximum when the RF momentum acceptance meets the lattice momentum acceptance. For higher RF voltages a shorter bunch length will lead to lower lifetime.

Fig. 12 displays the linear Touschek lifetime as a function of RF-voltage and the total lifetime including also elastic beam gas scattering and bremsstrahlung. Since there is a voltage limitation for the cavity of 650 kV, 3 cavities would be required to reach the maximum lifetime for Touschek scattering. On the other hand, if the total lifetime is considered, 2 cavities would be more than sufficient. But because of the low elastic beam gas scattering lifetime, Spiral COSAMI has to rely on frequent top-up injection anyway, therefore even 1 cavity only can be considered.

A further reduction of the lifetime is caused by the limitation of the momentum acceptance due to the nonlinearities of the lattice. Fig. 13 shows the linear and nonlinear momentum acceptance of the lattice. An improvement of the Touschek scattering lifetime could be reached by the implementation of an optional 3rd harmonic cavity which in turn would also reduce the emittance blow up due to Intra Beam Scattering (which was not included in the lifetime calculation). Such a cavity would reduce the charge concentration by a bunch lengthening of roughly a factor 2.5 and increase the total lifetime from 23 to 42 minutes in the nonlinear case. Space for cavity installation would be available in one of the transfer paths, however it may be questionable if the gain in lifetime warrants the additional investment and complexity, since frequent top-up is required anyway. So far, the most simple RF-system with only one fundamental RF-cavity is assumed.

The lifetime results and relevant parameters for the one-cavity case are collected in Table 2.

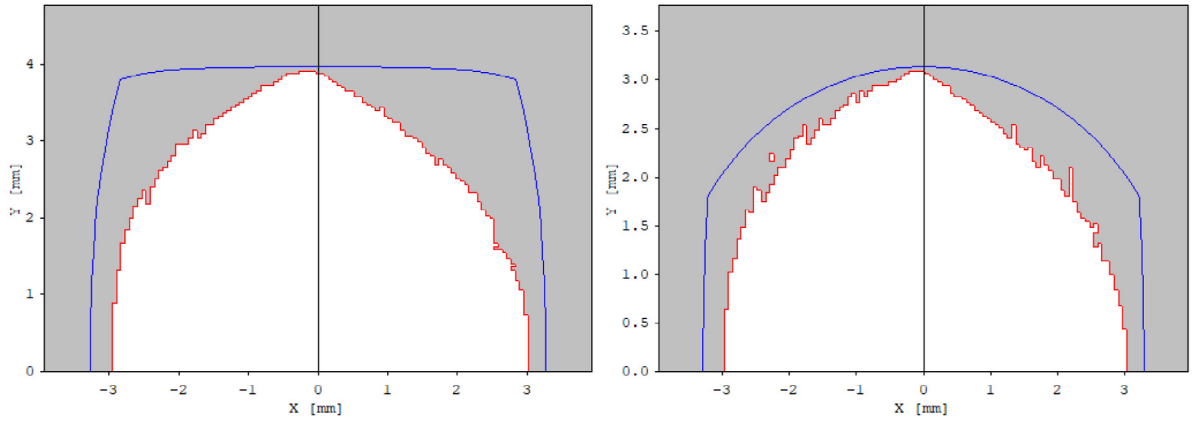

Fig. 11. Dynamic aperture for the symmetry point of the medium level undulator midpoint (β_x / β_y = 0.43 / 3.4 m). The blue contour shows the projection of the apertures to the trackpoint for a beam pipe of 30×20 mm^2 diameter, without (left) and with (right) undulator gaps of 6 mm. (For interpretation of the references to color in this figure legend, the reader is referred to the web version of this article.)

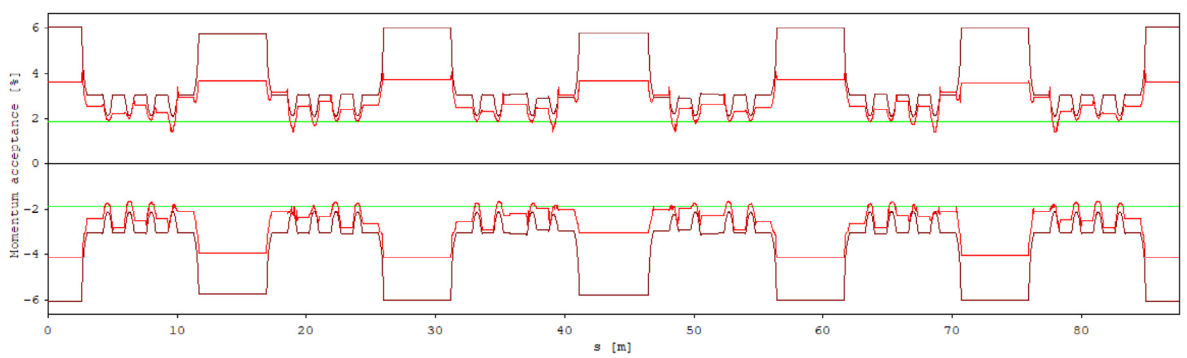

Fig. 13. Momentum acceptance. The horizontal (green) lines at ±1.9% show the RF acceptance, the outer (brown) lines the linear lattice acceptance determined by apertures, and the inner (red) lines the non-linear acceptance from tracking. (For interpretation of the references to color in this figure legend, the reader is referred to the web version of this article.)

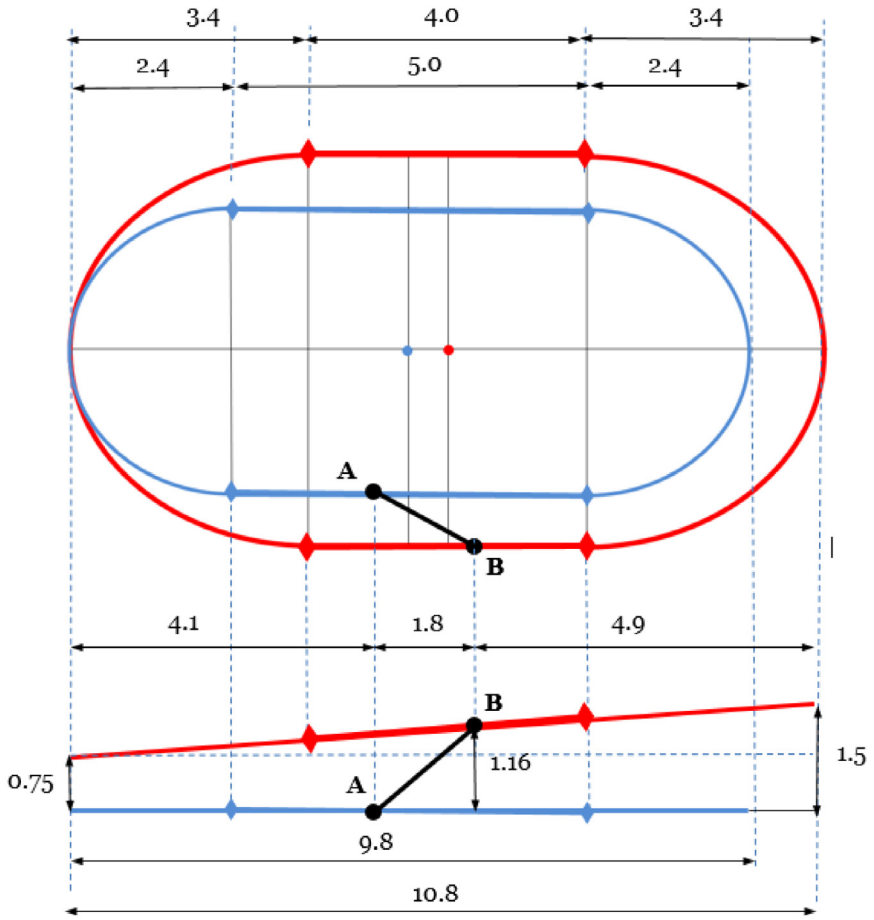

Fig. 14. Horizontal and vertical conceptual view of the booster extraction and storage ring injection layout. Longitudinal dimensions and vertical displacements are shown in m; the total length of the straights are 4 and 5 m for the booster and storage ring, respectively. The distance to the booster level, as well as the distance between loops is assumed to be 0.75 m.

7. Injection

An injection system is proposed here, where the beam is extracted from the booster by a septum tilted into the plane of transfer line and the straight sections of booster and storage ring.

The displacements generated by the fast injection kicker and sampled by the nonlinear injection kicker are purely horizontal. The booster is placed inside the storage ring area and shifted in longitudinal direction in order to relax the strengths of the injection elements. The pre-accelerator for the booster (either Linac or Microtron) will be located inside the booster area.

Fig. 14 shows the layout of the two accelerators. The deflection points of the septa are marked by black dots A and B which are also shown in the subsequent figures.

Fig. 15 shows the orientation of the transfer path from the booster septum deflection point A to the storage ring deflection point B. Both septa are rotated into the plane of the beam transfer. For the booster into the plane defined by the transfer path and the booster beam (blue) and for the storage ring into the plane defined by the transfer path and the Storage Ring beam (red).

Detailed views of the shadowed areas (not to scale transversely) are shown in Figs. 16 and 17. The injected beam has to be inside

Table 2
Beam lifetimes and relevant parameters.

Parameter	Unit	Value
Beam energy	MeV	430
Beam Current	mA	150
Number of bunches (~20% gap)		116
Harmonic number		146
Number of cavities		1
RF voltage	MV	0.65
Horizontal emittance	nm rad	3.4
Emittance coupling, ratio ϵ_y/ϵ_x	%	5.7
RF momentum acceptance	%	1.9
RMS bunch length	mm	3.8
RMS energy spread	10^{-4}	3.7
Vacuum pressure (assuming N_2)	pbar	2
Partial lifetimes:		
Elastic gas scattering[a]	h	0.94
Bremsstrahlung[a]	h	35.0
Touschek	h	0.33
Total lifetimes:		
Linear	h	0.24
Nonlinear	h	0.23

[a]Assuming CO/N_2 as residual gas.

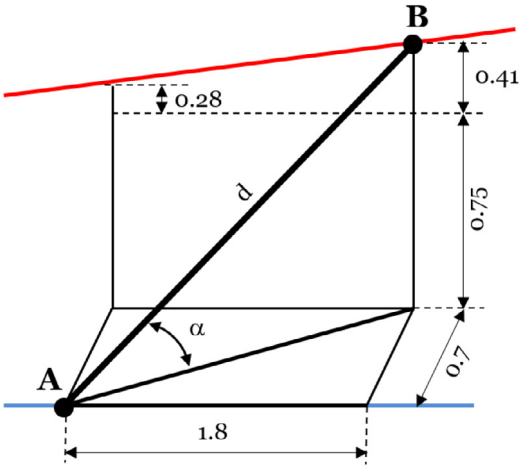

Fig. 15. Geometry of beam transfer. (For interpretation of the references to color in this figure legend, the reader is referred to the web version of this article.)

the dynamic aperture after the deflection by the nonlinear kicker. The horizontal value displayed in Fig. 11 has to be scaled by the square root of the beta values, which leads in the injection straight to an available horizontal dynamic aperture of 13 mm. The strengths of the injection elements are displayed in Table 3.

The injection process in phase space is displayed in Fig. 18. A pulsed sextupole is assumed for the nonlinear kicker.

8. Magnets

The basic magnet parameters are listed in Table 4. All magnet strengths are well within technical feasibility. Aperture radii of 24 mm were assumed for quadrupoles and sextupoles. For the combined function bending magnets, an effective pole width of ±24 mm was assumed to estimate the maximum pole tip field.

With the following definitions for the magnet strengths:

$$\Phi\,[\mathrm{rad}] = \frac{1}{B\rho} BL = \frac{0.3}{E\,[\mathrm{GeV}]} B\,[\mathrm{T}]\, L\,[\mathrm{m}];$$

$$K\,[\mathrm{m}^{-2}] = \frac{1}{B\rho}\frac{\partial B}{\partial x} = \frac{0.3}{E\,[\mathrm{GeV}]} B'\left[\frac{\mathrm{T}}{\mathrm{m}}\right] \quad B_p = B'R;$$

$$M\,[\mathrm{m}^{-3}] = \frac{1}{2}\frac{1}{B\rho}\frac{\partial^2 B}{\partial x^2} = \frac{1}{2}\frac{0.3}{E\,[\mathrm{GeV}]} B''\left[\frac{\mathrm{T}}{\mathrm{m}^2}\right] \quad B_p = \frac{1}{2}B''R^2$$

Table 3
Parameters of the injection elements.

Type	L [m]	Φ [mrad]	B [mT]
BO-KI	0.3	21.1	101
BO-LSE	1.0	610	556
SR-LSE	1.0	610	556
SR-NLK[a]	0.4	15.0	54

[a]Deflection at 7.5 mm radial position.

Table 4
Storage ring magnet parameters.

Type	No.	L [mm]	Φ [°]	K [m^{-2}]	M [m^{-3}]	B_p [T]
Lattice bending magnets (combined function magnets):						
BM	24	840	36	−2.619	−20.87	1.18
BMU	6	420	18	−2.136	−23.81	1.17
BMI	6	420	18	−2.019	−1.86	0.78
Straight section quadrupoles:						
QXU	6	100		18.995		0.65
QYU	6	100		−9.738		0.33
QXI	4	100		13.873		0.48
QYI	4	100		−8.142		0.28
QXR	2	100		13.854		0.48
QYR	2	100		−8.075		0.28
Cell quadrupoles:						
QS	36	0.1		17.116		0.59
		0.1				
		0.1				
		0.1				
QA1	6	100		16.847		0.57
QA2	6	100		13.977		0.48
QA3	6	100		16.718		0.57
QA4	6	100		14.118		0.48
Sextupoles						
SH	12	25			67.34	0.056
SFA	24	25			168.59	0.140
SFS	36	25			195.49	0.162
SD	12	25			−23.32	0.019

9. RF-system

The basic parameters of the storage ring relevant for the RF are listed in Table 5. The selection of the RF frequency is mainly dictated by the availability of commercial RF power sources and other components. An Elettra cavity [5] has been chosen here.

An RF voltage 0.65 MV is necessary in order to provide an acceptable lifetime for Touschek scattering, assuming a beam current of 150 mA and 110 buckets out of 146 filled. A gap of about 25% is introduced for ion clearing.

The total power required for the RF system is given by

$$P_o = P_b + P_c + P_l$$

with indices *b, c, l* referring, respectively, to beam power, power losses in the cavity and general losses in the waveguides including also the reflected power if the current does not correspond to the nominal current (for which the coupling factor is optimized).

In detail we have:

$$P_b = U_o I = (6.8\ \mathrm{kV}) \times (150\ \mathrm{mA}) = 1\ \mathrm{kW},$$

$$P_c = \frac{V_c^2}{2R_s} = \frac{(650\ \mathrm{kV})^2}{2\,(3.4\ \mathrm{M\Omega})} = 62.1\ \mathrm{kW}$$

$$P_l < 3\ \mathrm{kW}\ \text{(estimated)},$$

with V_C = 650 kV, the voltage per cavity, R_s = 3.4 MΩ, the shunt impedance of the (Elettra) cavity and eU_o = 6.8 keV, the energy due to synchrotron radiation per turn. Additional losses in the RF system in waveguides or due to reflected power from the cavity have been estimated to 3 kW.

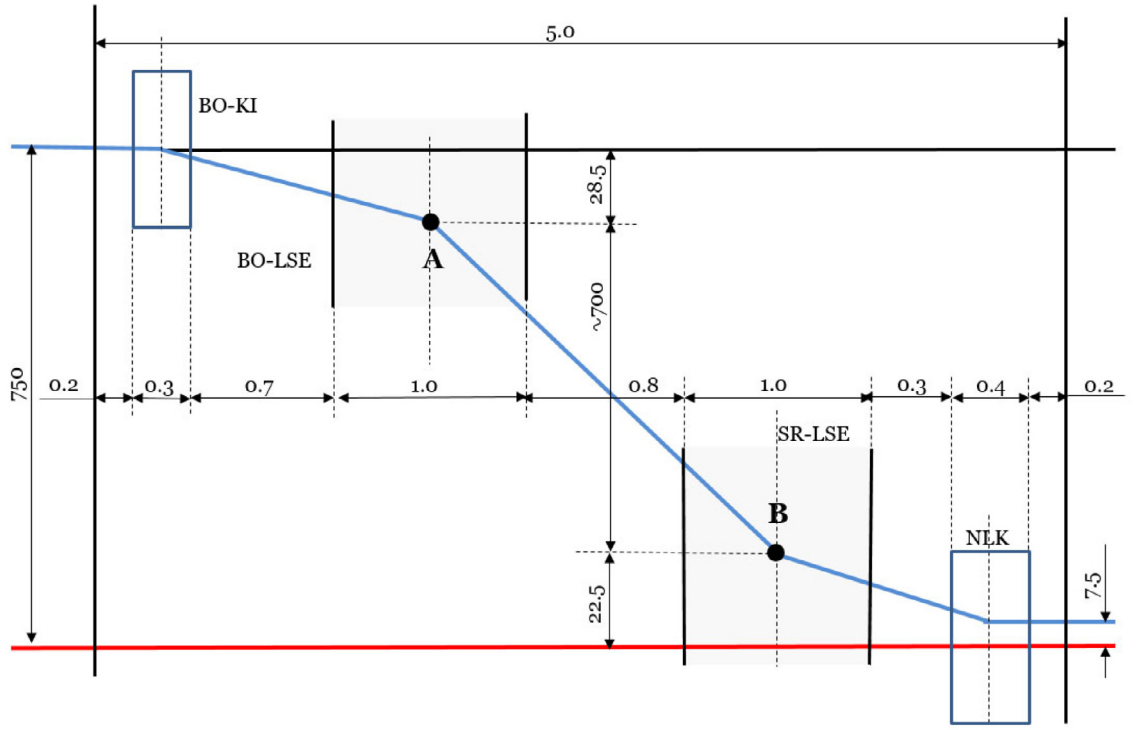

Fig. 16. Horizontal layout of the injection region with the booster and storage ring.

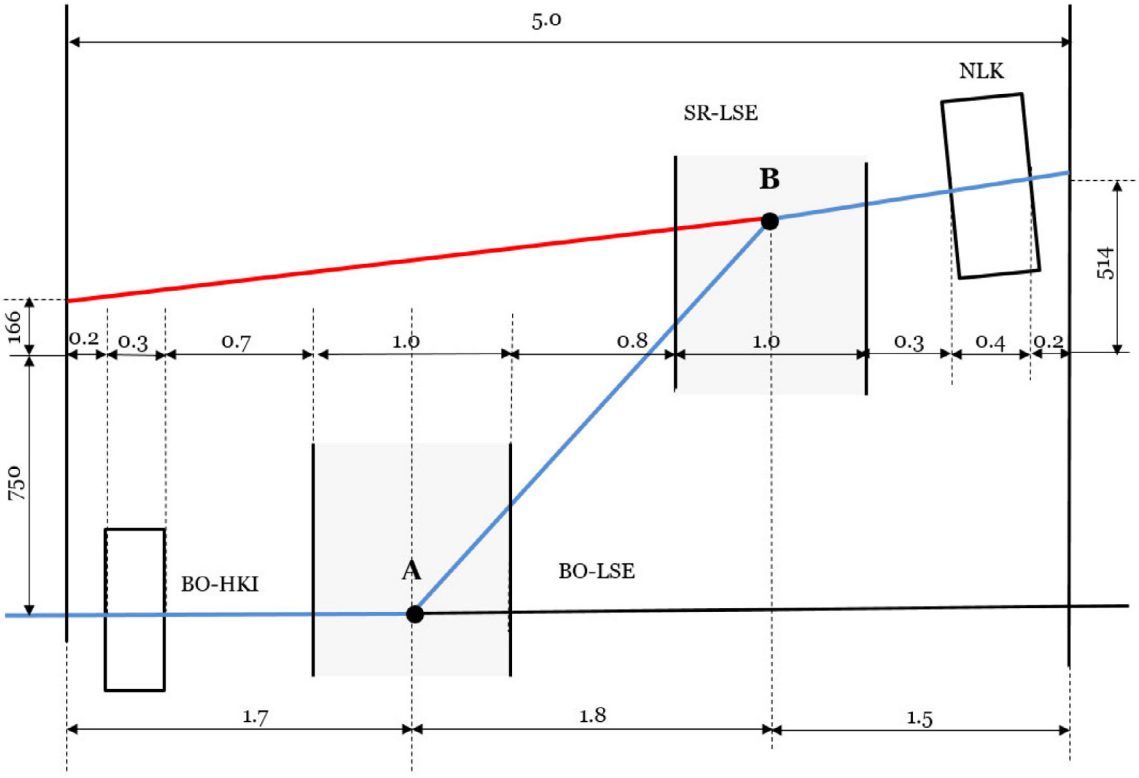

Fig. 17. Vertical layout of the injection region with booster and storage ring. The septa are only indicated as shadowed areas with dimension lines.

Most of the power is needed to generate a cavity voltage of 650 kV, whereas the power delivered to the beam (per cavity) is negligible. Therefore enough flexibility is guaranteed if the beam current should be increased in the future.

A total power of 66.1 kW is needed for one cavity. In order to have some margin for the power to be provided for the storage ring and taking into account an efficiency of the power system of 65 %, the power to be installed for the RF-system is roughly 110 kW. The final RF

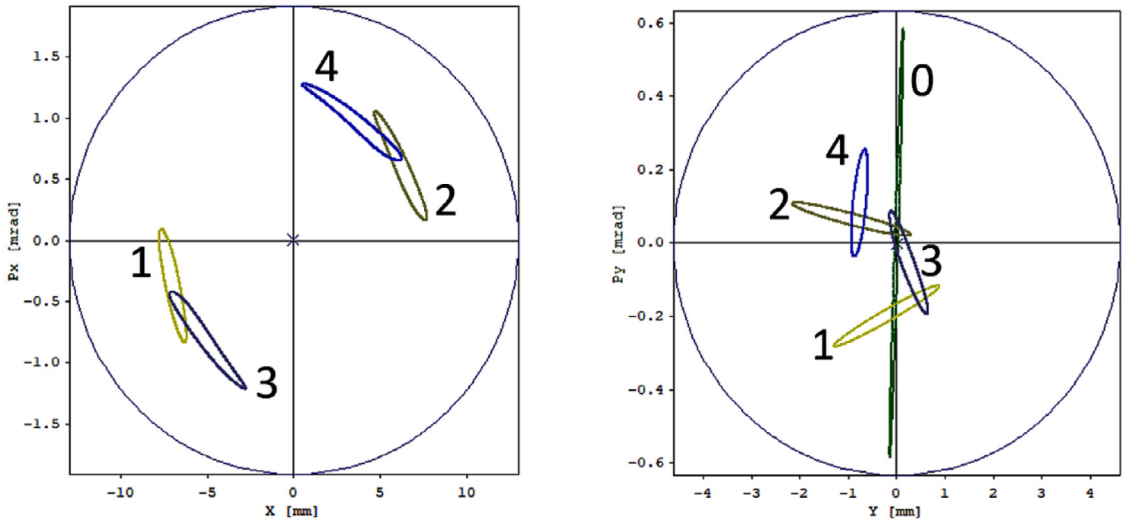

Fig. 18. Injection with an NLK (pulsed sextupole) providing a kick of 15 mrad at $x = 7.5$ mm. Left and right plots show the horizontal and vertical phase space of the injected beam (turn 0, outside plot range in horizontal phase space), and after the first four turns (turns 1,2,3,4). The enclosed area corresponds to emittances of 200 nm horizontal and 20 nm vertical. The beam is injected at $x_0 = 7.5$ mm, $x'_0 = -16$ mrad, $y_0 = 0$ mm, $y'_0 = 0$, and focused to $\beta_{x/y} = 1$ m and $\alpha_{x/y} = \pm 4$ in order to compensate the large local gradient of the pulsed sextupole.

Table 5
RF-parameters.

Parameter	Unit	Value
RF-Frequency	MHz	499.7
RF voltage	MV	0.65
Momentum acceptance	%	1.9
Number of cavities		1
Cavity shunt impedance	MΩ	3.4
Power to the beam	kW	1
Cavity wall losses	kW	62

parameters together with the relevant beam parameters are collected in Table 5.

The RF cavity could be placed in the upper transfer path or the return path.

10. Conclusions

With the spiral configuration three independent COSAMI-like beams could be generated for Actinic Mask Inspection. In this way splitting a single beam is avoided and therefore higher single beam powers can be achieved. It is a more economical solution than a setup with three independent devices. The obvious advantages are:

- The floor space is not larger than for a single COSAMI facility
- Only one injection system is required
- Only one RF-system is required
- Sophisticated diagnostics is implemented only once
- With respect to ion-trapping a higher current could be stored. For the same duty cycle the gap is 3 times as long and clearing becomes more efficient
- The requirement on pulse duration of the injection kicker is more relaxed.

The spiral configuration is particular attractive at relatively low beam energy, where magnets of large bending angle and short focal length are feasible and affordable. If the concept is scaled to higher beam energy in order to cover a wider wavelength range, it must be compared to a conventional, i.e. flat storage ring with same number of magnets but lower strength, lower emittance (since it scales with third power of bending angle per magnet), but three times larger circumference. For lower beam energy, as required for actinic mask inspection and similar applications in an industrial environment, the spiral COSAMI storage ring presents an unconventional and highly efficient solution in terms of performance, investment and space requirements.

CRediT authorship contribution statement

Albin F. Wrulich: Conceptualization, Methodology, Investigation, Writing – original draft. **Andreas Streun:** Methodology, Software, Investigation, Writing – review & editing. **Leonid Rivkin:** Conceptualization, Supervision.

Declaration of competing interest

The authors declare that they have no known competing financial interests or personal relationships that could have appeared to influence the work reported in this paper.

Funding statement

This research did not receive any specific grant from funding agencies in the public, commercial, or not-for-profit sectors.

Data availability statement

The data that support the findings of this study are available from the corresponding author upon reasonable request.

References

[1] T. Garvey, L. Rivkin, A. Streun, A. Wrulich, Y. Ekinci, A compact storage ring for the production of EUV radiation, in: Proc. ANS AccApp'17: 13th Int. Topical Meeting on the Applications of Accelerators, Quebec, Canada, 2017, http://accapp17.org/wp-content/2017/data/pdfs/130-23542.pdf.
[2] Y. Ekinci, T. Garvey, A. Streun, A. Wrulich, L. Rivkin, A high-brightness accelerator-based EUV source for metrology applications, in: Proc. SPIE 10810, Photomask Technology, Monterey CA, United States, 2018, 108100W, https://doi.org/10.1117/12.2501930.
[3] Y. Ekinci, A. Wrulich, L. Rivkin, A. Streun, A Compact Light Source for Metrology Applications in the EUV Range, WO2017036840A1, Paul Scherrer Institut, Switzerland, 2016, https://patents.google.com/patent/WO2017036840A1/en.
[4] A. Wrulich, L. Rivkin, A. Streun, A Multi-Undulator Spiral Compact Light Source, WO2018072913A1, Paul Scherrer Institut, Switzerland, https://patents.google.com/patent/WO2018072913A1/en.
[5] A. Massarotti, G.D'. Auria. A. Fabris, C. Pasotti, C. Rossi, M. Svandrlik, 500 MHz cavities for the trieste synchrotron light source ELETTRA, in: Proc. 2nd Europ. Part. Acc. Conf., Nice, France, 1990, pp. 919–921.